China Instrument and Control Society
Instrumentation
OPEN ACCESS
INSTRUMENTATION, Vol. 13, No. 3, September 2026 https://doi.org/10.15878/j.instr.202600399

Articles

SCCA-HRBF: A Structure Confidence-coupled Adaptive Hermite Radial Basis Function Method

Yunzhu Yang[1,2], Zhiyi Wang[1*], Jianli Wang[1,2], Changhua Liu[1,2], Shengbo Zhang[1,2], Zhengqi Sun[1,2]

[1] Electro-Optical Sensing Department, Changchun Institute of Optics, Fine Mechanics and Physics, Chinese Academy of Sciences, Changchun, Jilin 130033, China

[2] Daheng College, University of Chinese Academy of Sciences, Beijing 100049, China

Abstract: A structure confidence-coupled adaptive Hermite radial basis function (SCCA-HRBF) method is proposed for denoising precision optical measurement point clouds affected by random noise, local anomalous disturbances, and varying observation reliability. First, local curvature features are extracted using principal component analysis of neighboring regions, and an observation confidence model is constructed by integrating height and normal consistencies and local fluctuation information to evaluate the reliability of measured points. Subsequently, a structure confidence-coupling mechanism is established to jointly characterize local structural complexity and observation reliability, enabling adaptive prioritization of HRBF centers and nonuniform degree allocation for implicit surface reconstruction. Finally, point-value, gradient, and local structural consistency constraints are integrated within a weighted Hermite radial basis function framework to achieve continuous surface reconstruction, followed by point-cloud correction along the measurement direction. The proposed method is validated using real point-cloud data acquired from mosaic detector focal planes and compared with Gaussian filtering, bilateral filtering, moving least-squares (MLS), GeoGCN, Gaussian process regression (GPR), and Uniform HRBF. The results demonstrate the superior performance of SCCA-HRBF in terms of the root-mean-squared error (RMSE), mean absolute error (MAE), Peak-to-Valley (PV), Maximum Error (MAXE), and standard deviation (STD). Specifically, the RMSE and PV are reduced to 0.300688 μm and 1.186177 μm, respectively. Center-number and parameter sensitivity analyses verify the effectiveness of the proposed nonuniform degree allocation strategy and the method's robustness. These results indicate that the SCCA-HRBF effectively suppresses abnormal measurement disturbances and improves the accuracy and robustness of optical surface reconstruction, providing an effective data-processing approach for mosaic detector focal-plane inspection and precision optical surface measurements.

Keywords: point-cloud denoising; Hermite radial basis function; implicit surface reconstruction; structure confidence coupling; mosaic detector focal plane

Copyright: © 2026 by the authors. This article is licensed under a Creative Commons Attribution 4.0 International License (CC BY) license (https://creativecommons.org/licenses/by/4.0/).

Citation: Yunzhu Yang, Zhiyi Wang, Jianli Wang, Changhua Liu, Shengbo Zhang, Zhengqi Sun. "SCCA-HRBF: A Structure Confidence-coupled Adaptive Hermite Radial Basis Function Method. " Instrumentation 13, no. 3 (September 2026). https://doi. org/10.15878/j. instr.202600399

1 Introduction

High-precision three-dimensional surface measurement is extensively used in mosaic detector alignment, precision optical manufacturing, and large-aperture telescope focal-plane inspection[1-3]. Noncontact measurement

devices, such as spectral confocal displacement sensors, white-light interferometers, and laser profilometers, can rapidly acquire three-dimensional point-cloud data for surface reconstruction, flatness evaluation, and geometric error analysis[4-6]. However, in practical optical measurement systems, the acquired point-cloud data are typically affected by multiple types of uncertainties rather than a single homogeneous noise source. Specifically, these uncertainties can be categorized into several representative classes, including random measurement noise induced by sensor and optical signal fluctuations, outliers caused by transient acquisition failures or strong reflection artifacts, missing data resulting from signal loss or invalid sampling, surface discontinuities arising from abrupt geometric transitions or occlusions, and locally unreliable observations caused by unstable measurement conditions such as edge effects or low signal-to-noise ratios. Unlike conventional natural-scene point clouds, optical metrology data exhibit strong spatial correlations and systematic measurement characteristics, where different types of disturbances coexist and interact, significantly degrading surface reconstruction accuracy and robustness[7-10]. Therefore, the accurate recovery of the underlying surface from noisy point clouds remains a critical problem in precision optical metrology.

Unlike natural-scene point clouds, optical-measurement point clouds typically exhibit globally smooth variations with locally weak deformations. Most regions are smooth and only slight warpage and height deviations appear locally. In such cases, high-curvature regions are more vulnerable to measurement noise and normal fluctuations, resulting in reduced observation reliability. Consequently, denoising methods for optical measurement point clouds should simultaneously preserve the global surface smoothness, local weak structures, and robustness to complex noise.

Numerous point-cloud denoising methods based on geometric learning, graph optimization, probabilistic modeling, and implicit surface reconstruction have been recently proposed. Graph-based methods focus on exploiting local neighborhood structures to enforce geometric consistency. For instance, PathNet enhances local structural representation through adaptive path selection[11], whereas GeoGCN exploits both spatial and geometric features for robust denoising[12]. Mao et al. further integrate graph convolution with invertible neural networks to improve latent-space point-cloud recovery[13].

In implicit surface modeling, Wang et al. proposed an edge-preserving implicit representation for point clouds[14], and Xiao et al. introduced an alternating denoising and reconstruction framework for improving surface recovery quality[15]. Guo et al. further incorporated learned structural priors to enhance geometric preservation capability in point-cloud denoising tasks[16]. The classical Hermite radial basis function (HRBF) framework provides a unified implicit representation by combining positional and gradient constraints, enabling smooth and geometrically consistent surface reconstruction[17].

Beyond these approaches, recent studies have explored statistical and optimization-based denoising paradigms. Representative methods include K-means clustering with total Bregman divergence for robust point-cloud denoising[18], Gaussian process regression for probabilistic modeling of measurement uncertainty[19], and non-local optimization techniques such as curvature entropy and γ -norm minimization for enhanced robustness under complex noise distributions[20].

With the rapid development of deep learning, diffusion-based and neural generative models have also been widely studied. The P2P-Bridge diffusion framework formulates point-cloud denoising as a reverse stochastic diffusion process, achieving strong performance under severe corruption conditions[21]. Gradient-field-based methods model point evolution in continuous vector fields to improve reconstruction stability[22]. Classical architectures such as PointNet++ capture multi-scale geometric structures through hierarchical feature learning[23], while transformer-based models further enhance global dependency modeling via self-attention mechanisms[24].

Despite these advances, most existing methods are designed for natural-scene point clouds with irregular sampling distributions and complex semantic structures. In contrast, optical measurement point clouds exhibit globally smooth surfaces, weak local variations, and system-dependent structured noise. These differences limit the direct applicability of general-purpose methods in precision optical metrology scenarios, motivating the proposed SCCA-HRBF method.

2 Structure Confidence-coupled Measurement-constrained HRBF Point-cloud Denoising Method

2.1 Overall Framework

For precise optical surfaces, most regions typically exhibit smoothly varying low-curvature structures, with only slight warpage or weak local deformations. However, high-curvature regions not only require greater surface representation capability but are also more susceptible to edge effects, reflection instability, and normal-vector fluctuations, resulting in reduced observation reliability. Therefore, local structural complexity and observation stability are intrinsically coupled. Allocating reconstruction freedom solely according to the local curvature may erroneously interpret noisy regions as genuine structures, whereas adjusting constraint weights only according to observation stability may excessively smooth weak structural features. To address this issue, a structure confidence-coupling mechanism was established to

jointly regulate the local representation capability of the implicit surface according to the structural complexity and observation reliability, thereby enabling the nonuniform allocation of reconstruction freedom for optical measurement surfaces.

Based on this concept, the local curvature and normal distribution characteristics were first estimated using neighborhood-based PCA, and an observation-consistency model was constructed to evaluate local observation confidence. Subsequently, the distribution density of the HRBF centers was jointly determined using the normalized curvature and observation confidence. Finally, a weighted HRBF model was employed to reconstruct a continuous implicit surface, and a point cloud was projected along the optical measurement direction to obtain the final denoised result. The workflow of the proposed SCCA-HRBF method is illustrated in Fig. 1.

2.2 Local Structure Analysis and Observation Consistency Modeling

Before local structure analysis, a median absolute deviation (MAD) -based preprocessing step is applied to identify and remove isolated gross outliers according to the local height distribution. This preprocessing only eliminates evidently abnormal measurements, while the remaining random noise and locally unreliable observations are handled by the subsequent structure-confidence coupling and weighted HRBF reconstruction.

To characterize uncertainty in optical measurement point clouds, the observation consistency model is formulated by decomposing measurement errors into heterogeneous components, including random noise, outliers, missing data, surface discontinuities, and locally unreliable observations. These disturbances exhibit distinct geometric behaviors in space, leading to variations in local height and normal consistency. Accordingly, a unified metric is constructed to estimate point-wise reliability by jointly considering height variation, normal consistency, and structural stability. The point cloud is defined as follows.

The input point cloud is defined as $P=\{p_i=(x_i,y_i,z_i)\}_{i=1}^{N}$. For an arbitrary point p_i, the k-nearest neighbor set is defined as $\mathcal{N}_i=\{p_j\}_{j=1}^{K}$. The corresponding neighborhood centroid is $\bar{p}_i=\frac{1}{|\mathcal{N}_i|}\sum_{p_j\in\mathcal{N}_i}p_j$. The neighborhood covariance matrix is computed as

$$C_i=\frac{1}{|\mathcal{N}_i|}\sum_{p_j\in\mathcal{N}_i}(p_j-\bar{p}_i)(p_j-\bar{p}_i)^T \tag{1}$$

Eigenvalue decomposition is then performed on C_i,

$$\lambda_1\le\lambda_2\le\lambda_3 \tag{2}$$

where the eigenvector corresponding to the smallest eigenvalue is used as a local normal vector n_i. The local curvature indicator is defined as

$$K_i=\frac{\lambda_1}{\lambda_1+\lambda_2+\lambda_3} \tag{3}$$

This indicator reflects the degree to which the local region deviates from a planar surface. A smaller K_i value indicates a nearly flat region, whereas a larger value implies a more complex local geometry requiring higher surface representation capability.

As the original curvature measure may be sensitive to local noise and unstable edge sampling, the following normalization operation was applied:

$$\tilde{K}_i=\frac{\kappa_i-\kappa_{\min}}{\kappa_{\max}-\kappa_{\min}+\varepsilon} \tag{4}$$

where ε is a small stabilization constant.

An observation consistency model was constructed to evaluate the local observation reliability. The local mean height is first defined as

$$\bar{z}_i=\frac{1}{|\mathcal{N}_i|}\sum_{p_j\in\mathcal{N}_i}z_j \tag{5}$$

and the height-consistency error is given by

$$e_i^{(h)}=|z_i-\bar{z}_i| \tag{6}$$

The normal-consistency error is defined as

$$e_i^{(n)}=1-\frac{1}{|\mathcal{N}_i|}\sum_{p_j\in\mathcal{N}_i}|n_i^Tn_j| \tag{7}$$

When the neighborhood normals are highly consistent, the value of $e_i^{(n)}$ remains small. By contrast, a large value indicates considerable normal fluctuations, suggesting unstable observations or local anomalous disturbances.

The local height-fluctuation term is further defined as $e_i^{(\sigma)}=\sigma_i$, where

$$\sigma_i=\sqrt{\frac{1}{|\mathcal{N}_i|}\sum_{p_j\in\mathcal{N}_i}(z_j-\bar{z}_i)^2} \tag{8}$$

By combining the local statistical features above, the observation consistency error can be formulated as

$$e_i=\alpha_he_i^{(h)}+\alpha_ne_i^{(n)}+\alpha_\sigma e_i^{(\sigma)} \tag{9}$$

where α_h, α_n, and α_σ denote the weighting coefficients of different consistency terms.

Notably, Eq. (9) is computed entirely from the original point cloud and its local neighborhood statistics without relying on the implicit surface function to be reconstructed. Therefore, the observation weights can be estimated before the HRBF surface reconstruction, avoiding the circular dependency between the weight estimation and surface optimization.

Based on the observation-consistency error, the local observation confidence is defined as

$$w_i=\exp\left(-\frac{e_i^2}{2\tau^2}\right) \tag{10}$$

where τ is a scale parameter. When local observations are stable, w_i approaches 1. Conversely, for regions with unstable observations, the corresponding weight gradually decreases, thereby reducing the influence of low-confidence measurements on the subsequent surface reconstruction.

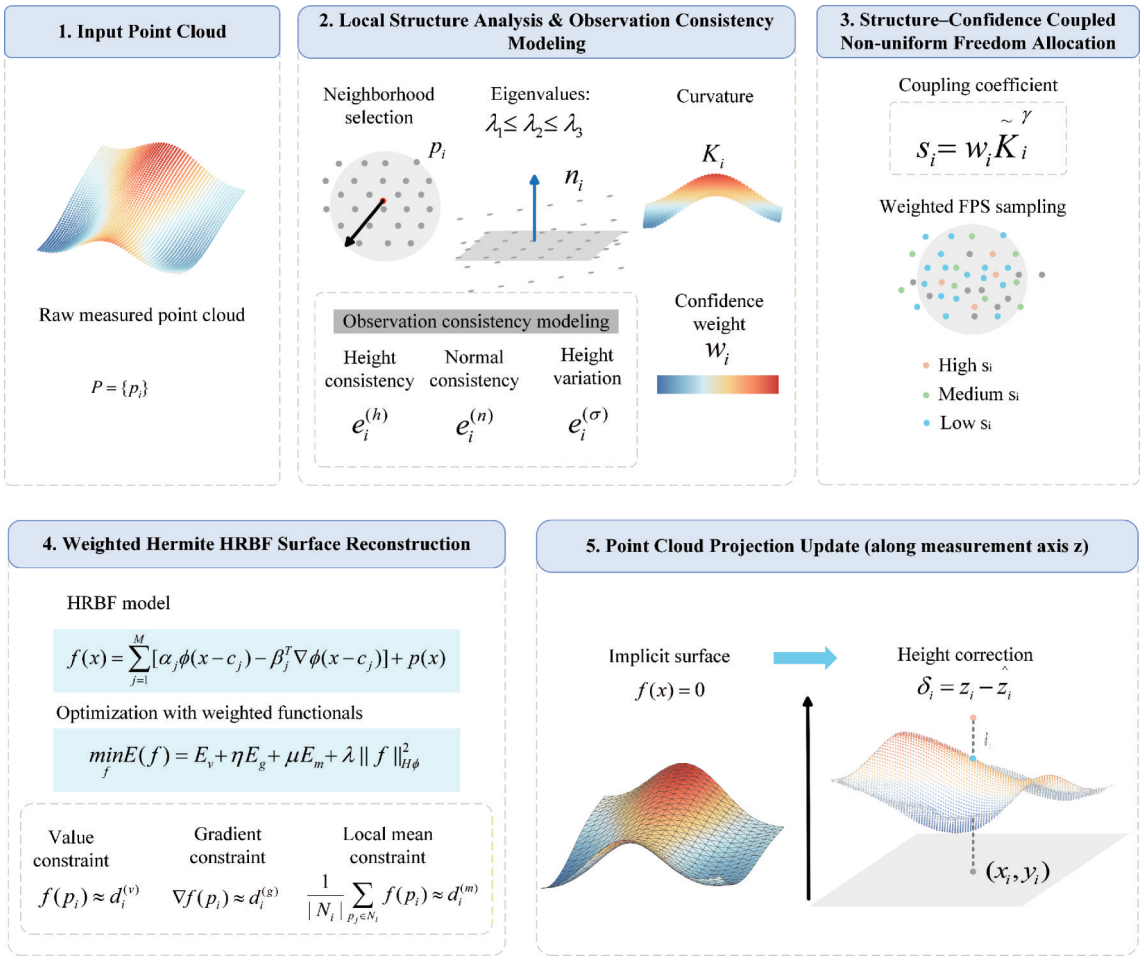


Fig.1 Framework of the proposed SCCA-HRBF method

2.3 Structure Confidence-coupled Nonuniform Degree-of-freedom Allocation

Conventional HRBF methods typically employ uniformly distributed centers for surface modeling. However, for optical measurement surfaces, large smooth regions typically require only a low level of surface representation capability, whereas local weak-structure regions require a higher local expressive power. A uniform degree-of-freedom distribution not only introduces redundant parameters in flat regions but may also lead to insufficient representation in geometrically complex areas.

Meanwhile, allocating the reconstruction freedom solely according to the local curvature also has limitations. As PCA-based curvature estimation is sensitive to random noise, large curvature values may originate from either genuine geometric structures or local disturbances, outliers, or unstable edge sampling. Consequently, curvature-only sampling strategies may emphasize noisy regions.

To address this issue, a coupling mechanism between the structural complexity and observation reliability is introduced. The structure confidence-coupling coefficient is defined as $s_i = w_i \tilde{K}_i^{\gamma}$, where γ is a curvature-adjustment parameter.

When a local region simultaneously exhibits high curvature and high observation confidence, a larger s_i value is obtained, indicating the presence of reliable structural information and thus requiring more HRBF representation freedom. In contrast, if a region has a high curvature, but the observation confidence is low, its sampling priority is suppressed, thereby reducing the influence of noise on the surface reconstruction.

Subsequently, a weighted farthest point sampling strategy is adopted to select the HRBF center set

$$C=\{c_j\}_{j=1}^{M}, M \ll N \tag{11}$$

During the jth sampling step, d_i denotes the shortest distance from point p_i to the currently selected center set. The new center is determined by

$$c_j = \arg\max_{p_i \in P} (s_i d_i) \tag{12}$$

Based on this strategy, dense sampling is performed in high-curvature and high-confidence regions; sparse sampling is applied in smooth regions; and sampling is suppressed in low-confidence regions, thereby achieving a nonuniform allocation of reconstruction freedom for optical measurement surfaces.

Based on the estimated observation confidence, the proposed structure-confidence coupling mechanism provides an adaptive response to different types of noise

and geometric disturbances in a unified framework. For regions with high-confidence and high-curvature structures, the model allocates increased degrees of freedom to preserve fine geometric details. In contrast, for low-confidence regions that are typically associated with outliers or unstable observations, the contribution of these points is adaptively suppressed during center selection and HRBF reconstruction, thereby mitigating their influence on the implicit surface.

For random measurement noise, the effect is implicitly reduced through the regularization behavior of the HRBF formulation. For missing or sparsely sampled regions, the reconstruction relies more heavily on neighboring structural information to maintain surface continuity. For surface discontinuities, the coupling mechanism prevents over-smoothing by preserving locally significant geometric variations when confidence remains sufficiently high. For locally unreliable observations, the reduced confidence weighting effectively limits their participation in both center selection and constraint formation. As a result, the proposed framework achieves a balanced trade-off between noise suppression and structure preservation under heterogeneous measurement conditions.

2.4 Weighted Hermite HRBF Surface Reconstruction

Compared with explicit surface models, implicit HRBF surfaces do not require predefined parameterization and are therefore more suitable for continuous surface reconstruction under weak local deformations and nonuniform structural distributions. Moreover, the HRBF framework can simultaneously incorporate positional and gradient constraints while naturally accommodating confidence-based adaptive weighting, rendering it particularly suitable for optical point-cloud reconstruction.

The implicit surface is represented as

$$f(x)=\sum_{j=1}^{M}\left[\alpha_j\phi(x-c_j)-\beta_j^T\nabla\phi(x-c_j)\right]+p(x) \quad (13)$$

where $\phi(x-c_j)=\phi(\|x-c_j\|)$ denotes the radial basis function kernel, $p(x)$ is a low-order polynomial term, and α_j and β_j are the coefficients associated with positional and gradient constraints, respectively.

In conventional HRBF formulations, an abnormal observation may directly affect the local implicit surface, thereby causing excessive attraction or oscillatory artifacts. As optical measurement surfaces are typically characterized by smooth and slowly varying structures, the implicit function response should remain stable within the local neighborhood. Therefore, a local structural consistency constraint is introduced to enhance neighborhood smoothness and reduce the influence of isolated abnormal observations.

Accordingly, the weighted HRBF optimization model is formulated as

$$\min_{f\in H_\phi}\frac{1}{2}\sum_i w_i^{(v)}\left|f(p_i)-d_i^{(v)}\right|^2+\frac{\eta}{2}\sum_i w_i^{(g)}\left\|\nabla f(p_i)-d_i^{(g)}\right\|^2+\frac{\mu}{2}\sum_i w_i^{(m)}\left|\frac{1}{|\mathcal{N}_i|}\sum_{p_j\in\mathcal{N}_i}f(p_j)-d_i^{(m)}\right|^2+\frac{\lambda}{2}\|f\|_{H_\phi}^2 \quad (14)$$

The first term enforces positional fitting, the second term corresponds to the Hermite gradient constraint for improving the local normal continuity, the third term enhances the local structural response stability, and the last term is the RKHS regularization term used to control the global surface complexity and suppress oscillations.

For positional and gradient constraints, the observation confidence is directly adopted as the weighting factor: $w_i^{(v)}=w_i$, $w_i^{(g)}=w_i$. For the local structural consistency constraint, the neighborhood-average confidence is employed:

$$w_i^{(m)}=\frac{1}{|\mathcal{N}_i|}\sum_{p_j\in\mathcal{N}_i}w_j \quad (15)$$

Based on this weighting mechanism, the influence of low-confidence observations is adaptively reduced, whereas reliable local structures are assigned higher representation capabilities during surface reconstruction.

2.5 Point-cloud Projection Update

By solving Eq. (14), the continuous implicit surface $f(x)$ can be obtained according to the following process. As the height information of optical measurement point clouds, such as those acquired by spectral confocal sensors, is primarily measured along the optical axis, a projection update strategy along the z direction is adopted.

For the original measurement point $p_i=(x_i,y_i,z_i)$, the lateral coordinates (x_i,y_i) are fixed and the zero-level set of the implicit surface is determined along the measurement direction $f(x_i,y_i,\hat{z}_i)=0,$, yielding the corrected height value $\hat{z}_i$.

As the projection direction is fixed along the measurement axis, the equation $f(x_i,y_i,\hat{z}_i)=0$ can be efficiently solved using a one-dimensional Newton iteration or bisection search along the z direction, resulting in a stable height correction.

The height deviation between the original measurement and the reconstructed surface is defined as $\delta_i=z_i-\hat{z}_i$. The final denoised point cloud is then obtained as $p_i^{new}=(x_i,y_i,\hat{z}_i)$.

Through projection updating along the measurement direction, random measurement noise and local anomalous disturbances can be effectively suppressed while preserving the overall continuity and local weak structural characteristics of the optical measurement surface.

3 Experimental Results and Analysis

3.1 Experimental Setup

To validate the effectiveness of the proposed SCCA-HRBF method, a self-developed XY raster scanning measurement system was constructed for three-dimensional point-cloud acquisition. The experimental platform consists of an in-house-developed scanning system incorporating an LMSD-SL-F310201-U610201×2-500-550×2-G001-A high-precision gantry stage (Shenzhen Han's Motor S&T Co., Ltd., Shenzhen, China), controlled by an EC-04040464NNNDNDNN SPiiPlus motion controller (ACS Motion Control, Yokne'am Illit, Israel), and a confocalDT IFS2405-3 spectral confocal displacement sensor with an IFC2421 controller (Micro-Epsilon Messtechnik GmbH & Co. KG, Ortenburg, Germany). The motion stage performs planar scanning, while the confocal probe provides high-resolution axial height measurements along the optical axis. The measured object is a mosaic detector focal plane sample with a physical size of approximately 16 mm × 16 mm. Data acquisition is performed using an XY grid scanning strategy with a uniform step size of 0.2 mm. Under identical experimental conditions, each sample is repeatedly measured 10 times to ensure statistical reliability and to evaluate the robustness of the proposed method.

During acquisition, each point in the point cloud is generated by synchronizing the stage position with the confocal sensor output, yielding a three-dimensional coordinate triplet (x, y, z), where the lateral coordinates are determined by the motion system and the height value is obtained from the optical measurement signal. To ensure consistency across repeated scans, a rigid registration procedure is applied prior to data fusion. Specifically, a Generalized Iterative Closest Point (GICP)-based registration method, implemented using the pcregistergicp function in MATLAB (version R2024a, MathWorks, Natick, MA, USA), is employed to achieve robust alignment under noisy and partially corrupted measurement conditions. For reference ground-truth measurements, a high-precision LUPHOScan 260 (Taylor Hobson Ltd., Leicester, UK) is used, providing a measurement accuracy of ±50 nm (3σ) and serving as the benchmark for quantitative evaluation.

The acquired point-cloud data are affected by multiple sources of uncertainty, including random noise induced by fluctuations in optical source intensity, local discontinuities and non-uniform sampling caused by encoder errors and synchronization inaccuracies between the motion stage and acquisition system, as well as low-amplitude disturbances introduced by environmental vibration and temperature variations. These factors collectively result in noisy and partially unreliable point-cloud measurements, posing significant challenges for subsequent surface reconstruction and analysis.

3.2 Quantitative Evaluation Results

To validate the effectiveness of the proposed SCCA-HRBF method for real optical measurement point-cloud denoising, comparative experiments were conducted using Gaussian filtering, bilateral filtering, moving least-squares (MLS), GeoGCN, Gaussian process regression (GPR), Uniform HRBF, and the proposed method. All methods were evaluated under identical datasets and consistent evaluation conditions. In this study, a single detector was measured using the proposed optical measurement system, and a high-precision LuphoScan system was subsequently employed to acquire the reference surface as the ground truth. The measured detector is shown in Fig.2.

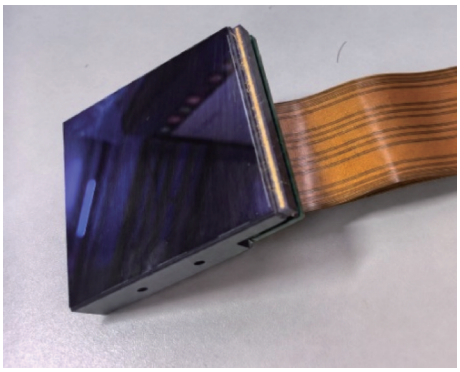


Fig.2 Photograph of the measured detector

The proposed SCCA-HRBF method achieved the best performance across all major error metrics (Fig. 3). On comparing it with Uniform HRBF, the root-mean-squared error (RMSE) decreases from 0.329961 μm to 0.300688 μm, corresponding to an improvement of approximately 8.9%. The Peak-to-Valley (PV) value decreases from 2.887628 μm to 1.186177 μm, representing a reduction of ~58.9%, while Maximum Error (MAXE) decreases from 1.933617 μm to 0.614981 μm, corresponding to a reduction of ~68.2%. The substantial improvements in PV and MAXE indicate that the proposed method effectively suppresses the influence of local abnormal measurements on surface reconstruction.

In addition to the quantitative results, Fig. 4 presents a visual comparison of the reconstructed surfaces obtained by different methods. It can be observed that the proposed SCCA-HRBF method achieves superior surface reconstruction quality, with better noise suppression and more accurate preservation of the underlying surface structure compared with the other competing methods.

The performance improvement mainly results from the proposed structure confidence coupling mechanism rather than simply increasing the complexity of the HRBF model. More reconstruction freedom is allocated to regions with rich structural information and high observation confidence, whereas regions with low observation reliability have fewer degrees of freedom.

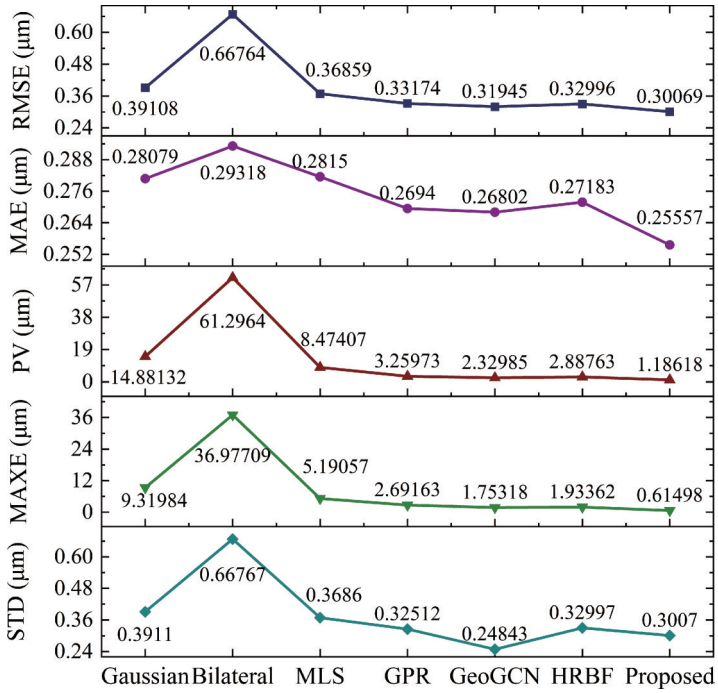


Fig.3 Comparison of Different Evaluation Metrics Obtained from Physical Experiments

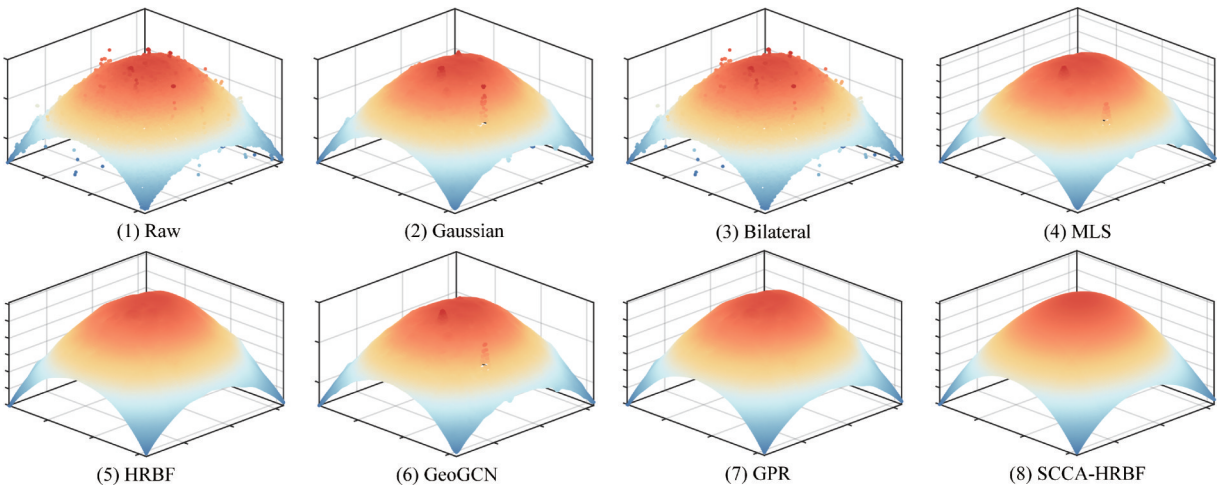


Fig. 4 Qualitative comparison of reconstructed surfaces using different point cloud denoising methods

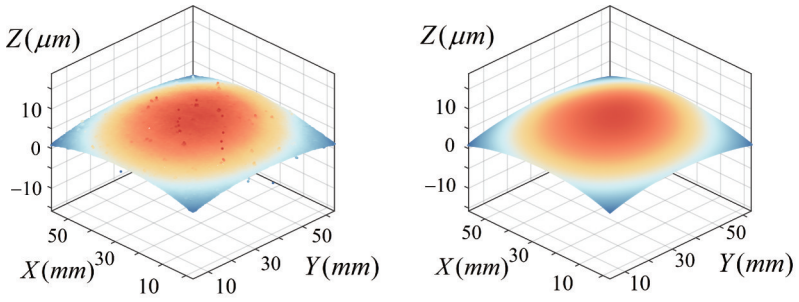
Consequently, the influence of abnormal observations on the implicit surface is reduced considerably. This enables the proposed method to preserve the overall surface continuity while improving the stability and robustness of local structure recovery.

3.3 Visualization Analysis of Point-cloud Denoising Results

To further evaluate the reconstruction performance of the proposed method, Fig. 5 presents a visual comparison between the original measured point cloud and the denoised result obtained by the SCCA-HRBF.

The original point cloud contains evident outliers and random disturbances (Fig. 5(a)). These abnormal observations appear as local protrusions, depressions, and high-frequency fluctuations on the surface, which not only degrade the surface continuity but may also introduce substantial errors in the subsequent flatness evaluation and surface-shape analysis. In addition, some outliers exhibited height deviations that substantially exceeded the overall surface variation range, indicating the coexistence of random noise and abnormal measurement errors.

After processing with the SCCA-HRBF (Fig. 5(b)), most isolated outliers were successfully removed, and the reconstructed surface exhibited a smoother and more continuous spatial distribution. Unlike conventional filtering methods that suppress noise through excessive smoothing, the proposed method selectively attenuates abnormal observations while preserving global surface trends. Consequently, the macroscopic geometric characteristics of the surface were maintained, whereas local high-frequency fluctuations were reduced considerably.



(a) Raw measured point cloud (b) SCCA-HRBF denoised point cloud

Fig.5 Three-dimensional surface visualization of the raw measured point cloud and the SCCA-HRBF denoised result

The visualization results were highly consistent with the quantitative evaluation results presented in Fig. 3. In particular, the substantial reductions in PV and MAXE directly correspond to the elimination of local protrusions and depressions, as observed in Fig. 5. These results demonstrate that the proposed structure confidence coupling strategy not only reduces overall reconstruction errors but also improves spatial consistency and geometric stability.

3.4 Sensitivity Analysis of the Number of Centers

To further evaluate the effectiveness of the proposed nonuniform degree-of-freedom allocation strategy, additional experiments were conducted to investigate the influence of the number of HRBF centers on the reconstruction performance. Five center numbers (100, 200, 300, 400, and 500) were tested, and the proposed SCCA-HRBF strategy was compared with the Uniform HRBF strategy. Figures 6 and 7 show the RMSE and PV variations, respectively.

As shown in Fig. 6, the RMSE values of both methods remained relatively stable as the number of centers increased. However, SCCA-HRBF consistently achieved lower RMSE values than Uniform HRBF under all test conditions. When only 100 centers were used, the RMSE of SCCA-HRBF reached 0.300374 μm, compared with 0.302097 μm for Uniform HRBF. Even when the number of centers increased to 500, Uniform HRBF failed to outperform SCCA-HRBF. These results indicate that the proposed method can utilize limited degrees of freedom more efficiently to achieve a higher reconstruction accuracy.

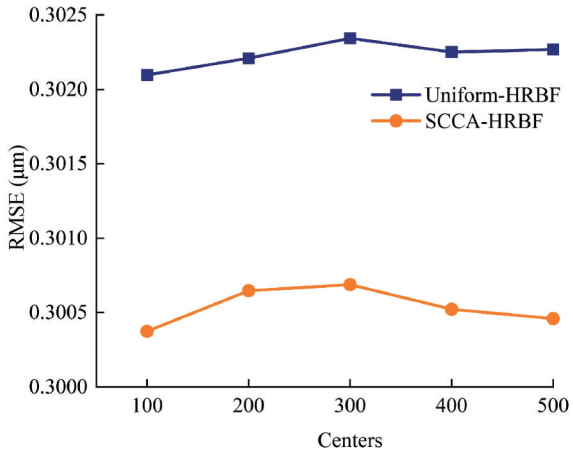


Fig.6 RMSE variation with the number of HRBF centers for Uniform HRBF and SCCA-HRBF

Fig. 7 shows that the PV values of both methods remained relatively stable across different center numbers. Nevertheless, the SCCA-HRBF exhibited smaller fluctuations and better stability over the entire test range. This demonstrates that the proposed center allocation strategy effectively prevents reconstruction freedom from being concentrated in abnormal regions, thereby reducing the influence of local measurement anomalies on the reconstructed surface.

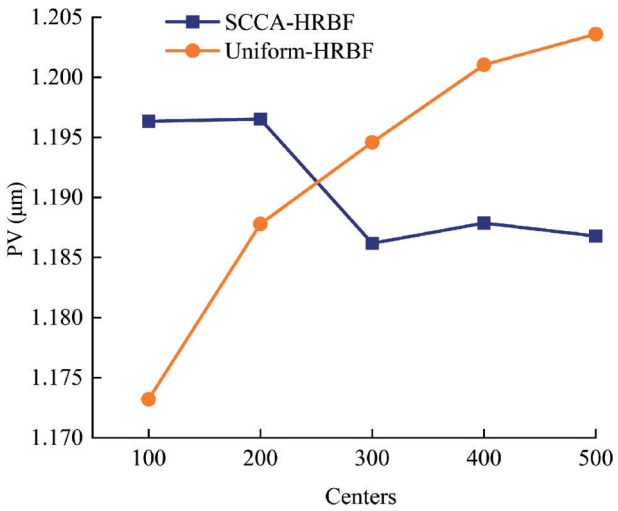


Fig.7 PV variation with the number of HRBF centers for Uniform HRBF and SCCA-HRBF

Increasing the number of centers from 100 to 500 changed the RMSE of the Uniform HRBF by less than 0.1%, indicating that simply increasing the number of centers cannot substantially enhance the reconstruction performance. In contrast, SCCA-HRBF achieved near-optimal performance even with a small number of centers. This suggests that the reconstruction performance depends more on the spatial distribution of the reconstruction freedom than on the total number of degrees of freedom.

These results confirm that the proposed structure confidence-coupling strategy enables a more reasonable allocation of reconstruction freedom by prioritizing

regions with rich structural information and reliable observations, thereby improving the overall surface reconstruction quality.

3.5 Parameter Sensitivity Analysis

The parameter γ controls the contribution of the structural term in the center-priority calculation and determines the balance between structural complexity and observation confidence. To investigate its influence, experiments were conducted with γ = 0.5, 0.8, 1.0, 1.2, 1.5, and 2.0. The corresponding RMSE and PV results are shown in Figs. 8 and 9, respectively.

When γ increases from 0.5 to 2.0, the RMSE changes minimally from 0.300451 μm to 0.302113 μm (Fig. 8), corresponding to a maximum variation of less than 0.6%. The performance curve remains stable without noticeable degradation, indicating that the proposed method is insensitive to parameter selection and exhibits strong robustness.

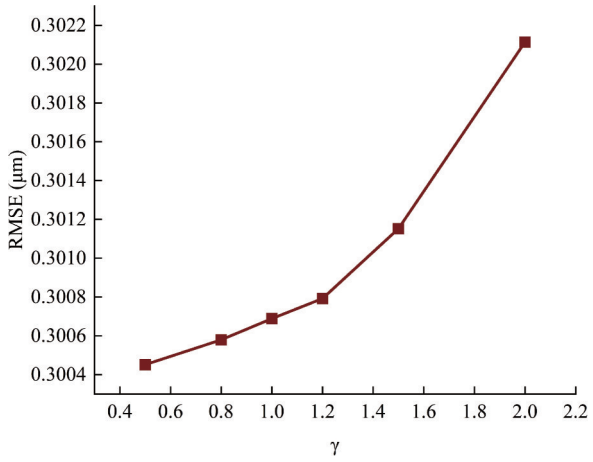


Fig.8 RMSE variation with different values of γ

The PV results shown in Fig. 9 exhibit a similar trend. Across all tested values of γ, the PV remains within the range of approximately 1.18-1.20 μm. Even under a strong structural enhancement condition, no obvious oscillation or abnormal amplification was observed on the reconstructed surface, demonstrating the stability of the proposed method.

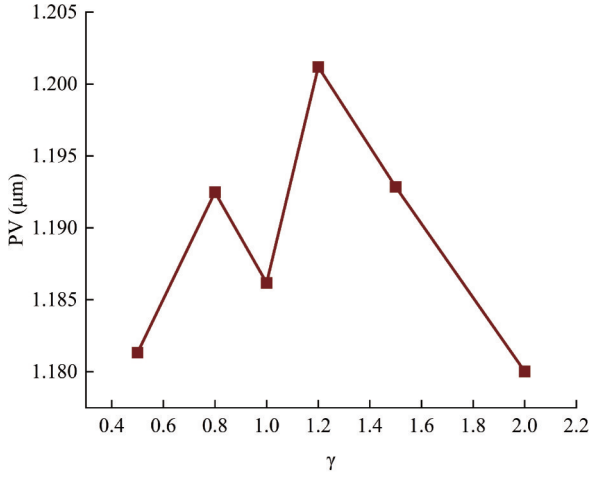


Fig.9 PV variation with different values of γ

From a physical perspective, when γ is small, the influence of structural complexity is weakened, and center allocation is primarily governed by observation confidence. As γ increases, regions with richer structural information gradually receive higher sampling priority. However, because observation confidence is simultaneously incorporated into the coupling mechanism, abnormal measurements cannot dominate the reconstruction process even at large γ values. This ensures the overall stability of the method.

Considering both the RMSE and PV results, the proposed method maintains a stable performance over a broad parameter range, demonstrating the robustness of the structure confidence-coupling mechanism. Taking reconstruction accuracy and model complexity into account, γ = 1.0 is selected as the default parameter in subsequent experiments.

3.6 Ablation Study

To further verify the effectiveness of each component in the proposed SCCA-HRBF framework, an ablation study is conducted by progressively disabling individual modules while keeping all other settings unchanged. The evaluated baseline variants include: (1) w/o MAD-based outlier suppression, (2) w/o local structure analysis (PCA-based curvature and normal consistency), (3) w/o structure-confidence coupled center selection, and (4) w/o local structural consistency constraint in HRBF reconstruction.

As shown in Table 1, removing any component leads to a noticeable degradation in reconstruction accuracy. In particular, eliminating the structure-confidence coupling strategy results in the most significant performance drop, especially in PV and MAXE metrics, indicating that uniform center allocation cannot effectively handle heterogeneous noise distributions in optical measurement point clouds. Similarly, disabling local structural consistency constraints leads to increased surface fluctuations, reflecting reduced smoothness in reconstructed results. When all components are integrated, the full SCCA-HRBF method achieves the best performance in all evaluation metrics, demonstrating the strong synergy among the proposed modules.

3.7 Summary

This section validates the proposed SCCA-HRBF method using actual optical measurement point-cloud data. Quantitative comparisons demonstrated that the proposed method achieved superior performance in terms of RMSE, MAE, PV, MAXE, and standard deviation (STD), indicating its effectiveness in suppressing random noise and local anomalies while improving the reconstruction accuracy.

The visualization results further confirmed that the proposed method effectively removed local outliers and

Table 1 Ablation study results of different components in SCCA-HRBF

MAD Outlier Removal	Structure Analysis (PCA)	Structure-Confidence Coupling	Local Consistency Constraint	RMSE (μm)	MAE (μm)	PV (μm)	MAXE (μm)	STD (μm)
√	√	√	√	0.300688	0.255571	1.186177	0.614981	0.3007
	√	√	√	0.3184	0.2691	1.4023	0.7426	0.3215
√		√	√	0.3276	0.2785	1.5892	0.8314	0.3389
√	√		√	0.3368	0.2861	1.7345	0.9126	0.3497
√	√	√		0.3219	0.2732	1.4587	0.7863	0.3304

high-frequency fluctuations while preserving the overall surface trend, thereby improving surface continuity and spatial consistency.

In addition, a sensitivity analysis of the number of HRBF centers verified the effectiveness of the proposed nonuniform degree-of-freedom allocation strategy, demonstrating that the structure confidence-coupling mechanism can allocate reconstruction freedom more efficiently.

Finally, parameter sensitivity experiments showed that RMSE and PV remained stable over a broad range of γ values, indicating strong robustness with respect to parameter selection.

Overall, the proposed SCCA-HRBF method effectively integrates structural information and observation reliability to achieve robust surface reconstruction for optical measurement point clouds, validating the effectiveness and practical potential of the proposed nonuniform degree-of-freedom allocation strategy.

4 Conclusion

This study presented an SCCA-HRBF point-cloud denoising method for precision optical measurement applications. By introducing a structure-confidence coupling mechanism into the HRBF reconstruction framework, the proposed method enables adaptive allocation of reconstruction freedom according to local geometric complexity and observation reliability. Experimental results demonstrated that the method achieves improved surface recovery accuracy and stronger suppression of local anomalous disturbances compared with conventional filtering and HRBF-based approaches.

Beyond the quantitative performance improvement, the proposed strategy provides a new perspective for optical measurement point-cloud processing. Instead of treating all observations equally, the method incorporates both structural characteristics and measurement reliability into the reconstruction process, allowing reconstruction resources to be distributed more effectively. This mechanism is particularly suitable for optical measurement scenarios characterized by globally smooth surfaces and locally weak deformations, such as mosaic detector focal planes and precision optical components.

Nevertheless, the current method still relies on locally estimated geometric features and does not explicitly incorporate optical surface priors or measurement physics. Its performance may therefore be affected when processing highly complex freeform surfaces or point clouds acquired under strongly nonuniform sampling conditions.

Future work will focus on integrating optical surface prior models, physical measurement constraints, and multi-scale geometric representations into the reconstruction framework. In addition, the extension of the proposed strategy to nonuniform scanning trajectories and multi-source measurement data will be investigated to further improve reconstruction accuracy, robustness, and practical applicability in precision optical metrology.

Author Contributions:

Yunzhu Yang: Conceptualization, Software, Writing-original draft; Zhiyi Wang: Conceptualization, Supervision, Writing-review & editing; Jianli Wang: Conceptualization, Methodology, Supervision, Funding acquisition, Resources; Changhua Liu: Investigation, Validation; Shengbo Zhang: Data curation; Zhengqi Sun: Data curation.

Funding Information:

This research was funded by the National Natural Science Foundation of China (grant numbers 12133009 [Key Program] and 12573084).

Data Availability:

The authors declare that the main data supporting the findings of this study are available within the paper and its Supplementary Information files.

Use of Generative AI and AI-Assisted Technologies

No generative AI was used.

Conflicts of Interest:

The authors declare no competing interests.

References

[1] Bezawada N., Haug M., Klein B., Brinkmann M., Müller E.,

Ives D., George E., Serra B., Alvarez D., Mehrgan L., Richerzhagen M., Seidel M., Stegmeier J., Todorovic M., Biondi F., Davies R., Emslander A., Sönmez A., Kravchenko K., Rabien S., Ziegleder J., Jilg T., & Neumeier L. (**2024**). The MICADO first light imager for the ELT: Overview of the near infrared mosaic detector subsystem. In X-Ray, Optical, and Infrared Detectors for Astronomy XI, *Proceedings of SPIE,* 13103, 131030D. doi:10.1117/12.3020079

[2] Catalucci S., Thompson A., Piano S., Branson III D. T., & Leach R. (**2022**). Optical metrology for digital manufacturing: A review. The International Journal of Advanced Manufacturing Technology, 120, 4271-4290. doi: 10.1007/s00170-022-09084-5

[3] Liu C. H., Guo N. X., Wang J. L., Chen T., Wu Z. Y., & Cheng X. (**2020**). Flatness measurement of a mosaic focal plane by using a coaxial multispectral laser. *Journal of the Korean Physical Society,* 77(8), 653-661. doi: 10.3938/jkps.77.653

[4] Jiao F., Liu L., Cheng W., Li C., & Zhang X. (**2022**). Review of optical measurement techniques for measuring three-dimensional topography of inner-wall-shaped parts. *Measurement,* 202, 111794. doi: 10.1016/j. measurement. 2022. 111794

[5] Zuo C., Qian J., Feng S., Yin W., Li Y., Fan P., Han J., Qian K., & Chen Q. (2022). *Deep learning in optical metrology: A review.* Light: Science & Applications, 11, 39. doi: 10.1038/s41377-022-00714-x

[6] Gao W., Haitjema H., Fang F. Z., Leach R. K., Cheung C. F., Savio E., & Linares J. M. (**2019**). On-machine and in-process surface metrology for precision manufacturing. *CIRP Annals,* 68(2), 843-866. doi:10.1016/j.cirp.**2019**.05.005

[7] Wang T., Wang Z., Yang Y., Mi X., Ti Y., & Wang J. (**2023**). A differential confocal sensor for simultaneous position and slope acquisitions based on a zero-crossing prediction algorithm. *Sensors,* 23(3), 1453. doi:10.3390/s23031453

[8] Wan M., Zheng R., Zhao H., & Yu L. (**2023**). Accuracy improvement of multi-view 3D laser scanning measurements based on point cloud error correction and global calibration optimization. Optics Express, 31(26), 42926-42944. doi: 10.1364/OE.509726

[9] Wang Z., Wang T., Yang Y., Yang Y., Mi X., & Wang J. (**2022**). Precise two-dimensional tilt measurement sensor with double-cylindrical mirror structure and modified mean-shift algorithm for a confocal microscopy system. *Sensors,* 22(18), 6794. doi:10.3390/s22186794

[10] Wang Z., Wang T., Yang Y., Mi X., & Wang J. (**2023**). Differential confocal optical probes with optimized detection efficiency and Pearson correlation coefficient strategy based on the peak-clustering algorithm. *Micromachines,* 14, 1163. doi:10.3390/mi14061163

[11] Wei Z., Chen H., Nan L., Wang J., Qin J., & Wei M. (**2024**). PathNet: Path-selective point cloud denoising. *IEEE Transactions on Pattern Analysis and Machine Intelligence,* 46(6), 4426-4442. doi:10.1109/TPAMI.2024.3355988

[12] Chen Z., Li P., Wei Z., Chen H., Xie H., Wei M., & Wang F. L. (**2023**). GeoGCN: Geometric dual-domain graph convolution network for point cloud denoising. *In Proceedings of the IEEE International Conference on Acoustics, Speech and Signal Processing (ICASSP* 2023), 1-5. doi:10.1109/ICASSP49357.2023.10094904

[13] Mao A., Yan B., Ma Z., & He Y. (**2024**). Denoising point clouds in latent space via graph convolution and invertible neural network. *In Proceedings of the IEEE/CVF Conference on Computer Vision and Pattern Recognition (CVPR* 2024), 5768-5777. doi:10.1109/CVPR52733.2024.00551

[14] Wang X., Cheng Y., Wang L., Lu J., Xu K., & Xiao G. (**2023**). Edge preserving implicit surface representation of point clouds. arXiv preprint arXiv: 2301.*04860*. doi: 10.48550/arXiv.2301.04860

[15] Xiao D., Shi Z., & Wang B. (**2023**). Alternately denoising and reconstructing unoriented point sets. *Computers & Graphics,* 116, 139-149. doi:10.1016/j.cag.2023.08.011

[16] Guo C., Liu Z., & He Y. (**2026**). Guiding point cloud denoising with learned structural priors. Proceedings of the AAAI Conference on Artificial Intelligence, 40(6), 4395-4402.

[17] Macêdo I., Gois J. P., & Velho L. (**2011**). Hermite radial basis functions implicits. *Computer Graphics Forum,* 30(1), 27-42. doi:10.1111/j.1467-8659.2010.01785.x

[18] Duan X., Mu A., Zhao X., & Wu Y. (**2025**). A K-means clustering algorithm with total Bregman divergence for point cloud denoising. *Symmetry,* 17(8), 1186. doi: 10.3390/sym17081186

[19] Kim I., & Singh S. K. (**2025**). 3D point cloud denoising via Gaussian processes regression. *The Visual Computer,* 41(12), 10481-10496. doi:10.1007/s00371-025-04049-7

[20] Chen J., Gao F., Chen P., & Lin W. (**2025**). Efficient non-local point cloud denoising using curvature entropy and γ-norm minimization. *IEEE Transactions on Visualization and Computer Graphics,* 31(10), 8738-8754. doi: 10.1109/TVCG.2025.3577915

[21] Vogel M., Tateno K., Pollefeys M., Tombari F., Rakotosaona M.-J., & Engelmann F. (**2025**). P2P-Bridge: Diffusion bridges for 3D point cloud denoising. *In Computer Vision - ECCV* 2024, LNCS 15060, 184-201. doi:10.1007/978-3-031-72627-9_11

[22] Hu Q., & Hu W. (**2025**). Dynamic point cloud denoising via gradient fields. *ACM Transactions on Multimedia Computing, Communications and Applications,* 21(4), 132. doi: 10.1145/3721431

[23] Qi C. R., Yi L., Su H., & Guibas L. J. (**2017**). PointNet++: Deep hierarchical feature learning on point sets in a metric space. *Advances in Neural Information Processing Systems,* 30. doi:10.48550/arXiv.1706.02413

[24] Wu X., Lao Y., Jiang L., Liu X., & Zhao H. (**2022**). Point Transformer V2: Grouped vector attention and partition-based pooling. *Advances in Neural Information Processing Systems,* 35. doi:10.52202/068431-2415